Materials Today Advances 28 (2025) 100648

Contents lists available at ScienceDirect

Materials Today Advances

journal homepage: www.journals.elsevier.com/materials-today-advances/

Tailoring self-propagating reaction dynamics in Ni/Al reactive multilayer foils via laser micromachining

Maria Amélia Martins [a,*], Christian Singer [b], Tim Dahmen [b,c], Frank Mücklich [a], Christoph Pauly [a]

[a] Chair of Functional Materials, Saarland University, 66123, Saarbrücken, Germany
[b] German Research Center for Artificial Intelligence GmbH (DFKI), Saarbrücken, 66123, Germany
[c] Hochschule Aalen, Technik und Wirtschaft, 73430 Aalen, Germany

ARTICLE INFO

Keywords:
Ultrashort pulsed laser
Laser micromachining
Self-propagating reaction
Reaction tailoring
NiAl
Reactive multilayer
Image analysis

ABSTRACT

Reactive multilayer foils (RMFs) offer highly localized heat generation through self-propagating exothermic reactions, making them attractive for advanced bonding applications. However, controlling the spatial and temporal distribution of heat remains a challenge. This study investigates the use of femtosecond laser micromachining to tailor the reaction dynamics of commercial Ni/Al reactive multilayer foils through the introduction of geometrical patterns. Four designs were chosen to impose distinct constraints on the reaction front. High-speed imaging combined with a custom image analysis algorithm enabled frame-by-frame tracking of local velocity fields. The results show that laser structuring can significantly alter reaction dynamics and propagation behavior by introducing front redirection, splitting and merging, leading to controlled delays and spatially localized acceleration zones. These effects enable modulation of global reaction times and localized energy release without suppressing or disrupting continuous front propagation. The findings demonstrate that laser structuring is an effective tool for tailoring heat delivery in RMF-based systems, with direct relevance to advanced bonding processes and thermally sensitive materials.

1. Introduction

Reactive metallic multilayer foils (RMFs), composed of alternating nanoscale metal layers such as Ni and Al, can undergo highly exothermic self-propagating reactions upon local ignition [1–8]. These energetic materials release significant heat in the millisecond range, achieving reaction front velocities ranging from 1 to 100 m/s and peak temperatures exceeding 2000 °C, depending on the specific system and bilayer thickness [2,9,10]. These properties make RMFs ideal for localized thermal applications, including reactive joining of temperature-sensitive materials, and ignition [8,11–17]. In particular, the Ni/Al system has been widely studied due to its high energy density and reproducibility as a commercial product [18–21]. The reaction mechanism is driven by the formation of intermetallic phases with a large negative enthalpy of formation [22], and the propagation dynamics are highly sensitive to both material properties and geometrical features.

In recent years, ultrashort pulsed (USP) laser micromachining has emerged as a promising technique for modifying geometries of sensitive materials such as RMFs with micrometer precision and minimal thermal damage [23–30]. Femtosecond laser structuring enables high-quality ablation without triggering the self-propagating reactions [31–33], allowing for complex patterning of the RMF. While earlier studies focused on characterizing laser-induced changes in microstructure and the extent of heat-affected zone (HAZ) [26,34], patterning can also be employed to strategically tailor reaction dynamics [35].

The spatio-temporal distribution of heat release during the reaction is largely governed by the geometry of the RMF sample, as demonstrated by recent studies showing that surface morphology, periodic structuring and thermal coupling with the substrate can significantly influence local propagation dynamics and energy transfer [36–39]. Surface morphology modifications, including periodic structuring and interfacial roughness, have been shown to influence propagation velocities by factors of 2–3 and induce transition from steady to oscillatory or spinning propagation modes [40]. By introducing designed patterns such as trenches and cut-outs, it is possible to manipulate the reaction front propagation in a controlled manner, opening new pathways for tailoring the thermal

* Corresponding author.
E-mail address: maria.martins@uni-saarland.de (M.A. Martins).

https://doi.org/10.1016/j.mtadv.2025.100648
Received 6 September 2025; Received in revised form 20 October 2025; Accepted 24 October 2025
Available online 5 November 2025

profile during ignition and propagation. Previous work has shown that external crack initiation by straining reactive Ni/Al multilayers on a substrate can significantly affect the propagation velocity and front morphology [41]. However, these studies were primarily focused on supported foils, substrate-induced effects, or simulation-based predictions. A systematic experimental evaluation of how specific geometrical patterns influence the reaction dynamics on free-standing foils has remained limited.

The ability to control spatio-temporal heat delivery through geometrical design addresses challenges in advanced manufacturing applications. In microelectronics packaging, precise thermal management is essential for joining dissimilar materials without damaging temperature-sensitive components [42]. Aerospace applications require controlled joining of lightweight alloys and composites where conventional welding creates considerable HAZ. The capability to program thermal profiles through geometric patterning represents a shift from reactive multilayers as passive heat source to active, spatially controlled thermal management systems.

Previous studies have demonstrated chemical or architected modifications in thermite systems to control reaction behavior [43,44]. However, experimental validation of geometry-induced tailoring in commercial free-standing Ni/Al foils has remained limited. The present study establishes geometrical structuring as a complementary and composition-independent path for controlling heat delivery in reactive multilayers.

By introducing patterns that influence the global and local dynamics of the reaction front, it is possible to control how heat is delivered and distributed throughout the foil. The investigated patterns influence both the duration and spatial distribution of the reaction. Reaction times are generally extended across all geometries, while localized thermal accumulation emerges in specific regions due to directional changes, confinement, and front splitting and merging. In practice, most patterns show a combination of these effects, with varying degrees of temporal extension and spatial redistribution. This capability to modulate both the duration and spatial profile of the thermal output is particularly relevant for future bonding technologies, where precise control of heat delivery can enhance joint quality, reduce thermal damage, and expand material compatibility. Four representative patterns were investigated: a square-shaped Double C, Vertical Line Arrays with 0.2 mm (VL-0.2) and 0.8 mm (VL-0.8) line spacing, and a Maze pattern. Each was designed to impose distinct spatial constraints on the front, such as redirection, splitting, merging, or periodic modulation. An unstructured foil served as the reference.

To quantitatively assess the influence of each geometry, a custom image analysis method was implemented. The source code of the method is provided as supplementary material. High-speed video recordings of the reaction were processed frame by frame to extract local velocity data. This approach provides a spatially resolved evaluation of front propagation dynamics and enables a more precise correlation between geometrical features and reaction behavior compared to traditional manual velocity measurements, thus providing a deeper understanding of heat propagation mechanisms.

2. Materials and methods

2.1. Sample preparation and laser micromachining

Commercial free-standing Ni/Al Nanofoil® reactive multilayer foils (Indium Corporation, Clinton, NY, USA) were used as the base material. These RMFs consist of alternating nickel and aluminum layers with bilayer thickness of 50 nm and a total foil thickness of 40 μm. A 1 μm thick InCuSil™ layer (61.5 wt% Ag, 24 wt% Cu, 14.5 wt% In) was present on both sides of the foils. The Ni:Al atomic ratio of 1:1 enables self-propagating reactions that produce peak temperatures between 1350 and 1500 °C and typical reaction front velocities of 6–8 m/s, according to manufacturer specifications [45].

The foils were cut into 10 mm × 15 mm rectangles and mounted on a computer-controlled 3-axis translation stage. Femtosecond laser micromachining was conducted using a Solstice® ACE™ Ti:Sapphire laser system (Spectra-Physics, Santa Clara, CA, USA), emitting 150 fs pulses at 800 nm wavelength and 1 kHz repetition rate. A 26 mm focal length aspheric lens focused the beam to a spot size of approximately 50 μm, achieving a fluence of 1.19 J/cm^2 with a pulse energy of 27 μJ. Structuring was conducted in ambient air using a vacuum-based debris extraction system to minimize oxide redeposition, as illustrated in Fig. 1a, which shows the stage, optical path and sample fixturing. The laser was operated with a scan speed of 0.02 mm/s in a single-pass direct laser writing mode. Multiple geometrical patterns were designed and fabricated by direct laser writing to locally modify the reaction front propagation. After micromachining, the samples underwent ultrasonic cleaning in ethanol for 1 h to remove loose particles and debris, as shown in Fig. 1b.

All samples in this work were produced from the same sheet of Nanofoil® to ensure comparable material properties, although small local variations within the sheet cannot be completely excluded. As is common when working with thin films, the samples went through several preparation and handling steps, such as laser structuring and transfer to the reaction test rig, during which small variations between samples may also naturally arise.

Given the delicate handling of free-standing foils, and the multiple preparation steps required, one representative sample was analyzed by geometrical pattern. The unstructured standard sample was tested multiple times and showed consistent results, supporting the reproducibility of the setup. Furthermore, each structured sample includes a pre-structure region that serves as reference, expressed by the normalized velocity (v/v_{pre}). The image analysis algorithm provides frame-by-frame, spatially resolved velocity data, which allows local variations to be detected and quantified with high precision, thereby reducing reliance on global averages.

2.2. Reaction recording

To initiate the exothermic reaction, the free-standing samples were clamped in a caliper-based test rig and ignited via electric spark. The reaction was recorded using a FASTCAM SA-Z 2100K high-speed camera (Photron, Tokyo, Japan) equipped with a 100 mm Macro 1x zoom lens. The camera was operated in a top-view configuration at 100k frames per second with a resolution of 640 x 280 pixels and a shutter speed of 0.35 μs. The optical setup provided a pixel size of 20 μm, corresponding to a total field of view of 13 × 6 mm^2. The camera was positioned to fully capture the structured region of each sample (16 mm^2) throughout the entire reaction.

2.3. Surface and microstructure characterization

A LEXT OLS4100 Confocal Laser Scanning Microscope (CLSM), Olympus (Shinjuku, Tokyo, Japan) was used for surface imaging in both optical and laser modes. High-resolution microstructural analysis was performed using a Helios G4 PFIB CXe scanning electron microscope/focused ion beam (SEM/FIB), ThermoFisher (Waltham, MA, USA), allowing detailed inspection of the morphology.

2.4. Image-based local velocity tracking algorithm

A custom image analysis algorithm named PropaTrack was developed and implemented to analyze the high-speed video data of the self-propagating reactions. The algorithm processed each frame to detect and track the position of the reaction front with high spatial and temporal precision. This method improves traditional tracking by leveraging advanced optical flow techniques and shape recognition.

The workflow consists of the following steps:

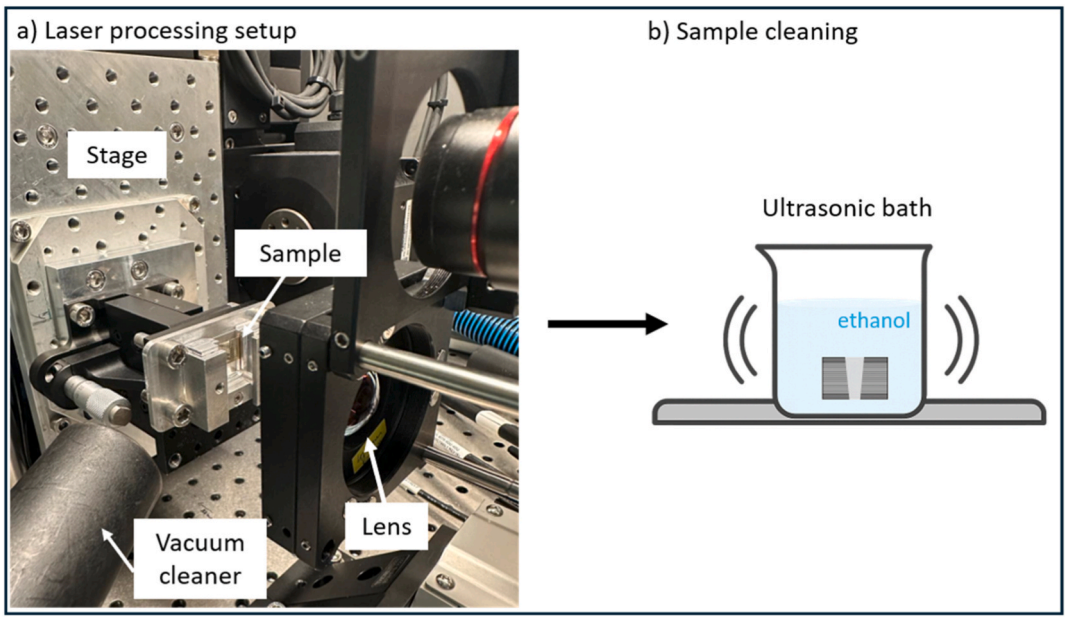

Fig. 1. – a) Experimental setup for femtosecond laser micromachining showing the optical path, focusing lens, sample mounting on the 3-axis translation stage, and vacuum-based debris extraction system. Corresponding laser parameters are: 26 mm focal length, 50 μm spot size, and 0.02 mm/s scan speed. b) Schematic of the post-processing ultrasonic cleaning of the structured Ni/Al foil in ethanol.

1. **Preprocessing**: High-speed video recordings were converted into grayscale image sequences and subjected to noise reduction using Gaussian filtering. Frames were then binarized using a fixed threshold to isolate thermally bright regions associated with the reaction front. Morphological operations, including closing and skeletonization were applied to remove small artifacts and ensure a one-pixel-wide front line [46].
2. **Front detection**: For each frame, the reaction front was detected using the Canny edge detector [47], which identifies regions of rapid intensity change. Static structures, such as post-reaction glow, were removed by comparing the current frame with its neighboring frames. Only features moving consistently over time were retained as reaction fronts.
3. **Spline fitting**: Detected fronts were converted into contours and fitted with cubic B-splines to model their shape smoothly [48]. This allows normal vectors to be calculated at multiple evenly spaced points along the front. The spline fit was essential to achieve sub-pixel accuracy and maintain continuity across frames.
4. **Velocity calculation**: To estimate local velocities, each spline point in the current frame was paired with the nearest point on the front in the subsequent frame. The displacement vector between corresponding points was projected onto the local normal vector to determine the propagation velocity. The results were saved as a vector field describing both direction and velocity. The PropaTrack outputs correspond directly to the field of view of the high-speed camera recordings. All velocity-fields analyses were therefore performed using a calibrated field of view of 13 × 6 mm^2. For the separate validation tests shown later in Section 3.3, a higher-magnification optical setup was used, corresponding to a field of view of 0.8 × 0.4 mm^2. Fig. 2 shows the vector field for one of the patterns used in this work.

A schematic overview of the image analysis pipeline is shown in Figs. 3 and 4, illustrating the steps involved in front detection and velocity estimation, respectively.

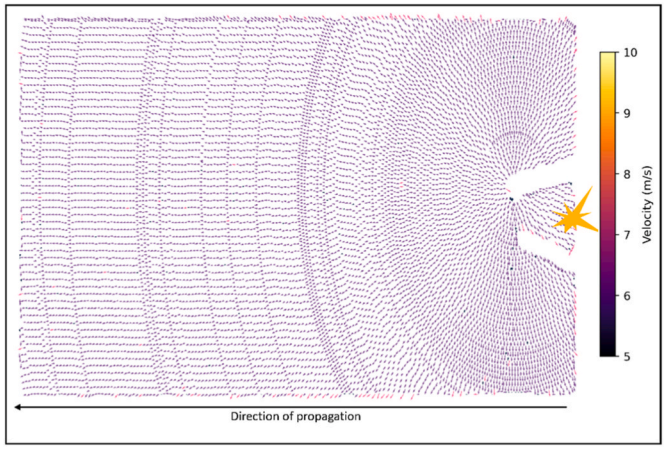

Fig. 2. Example of a vector field generated by PropaTrack for the Standard sample. The arrows indicate local reaction front direction, and their density highlights areas of strong directional change. Color intensity reflects local velocity magnitude, with red corresponding to the faster regions. The yellow spark represents the ignition point. Field of view is 13 × 6 mm^2 (same field of view of high-speed videos).

3. Results and discussion

3.1. Overview of micromachined patterns

To investigate how individual geometric features influence the dynamics of self-propagating reactions in Ni/Al RMFs, several laser micromachined geometries were initially tested. Based on preliminary observations, four patterns were selected for detailed analysis: Double C, Maze, Vertical lines with 0.2 mm line spacing (VL-0.2) and Vertical lines with 0.8 mm line spacing (VL-0.8). Here, "vertical" refers to the orientation of the laser-cut trenches relative to the net propagation direction. Each of these patterns were fabricated using femtosecond laser ablation and designed to impose different constraints on the reaction front.

Fig. 5 shows the top-view micrographs of the four selected structures. The Double C and the Maze structures introduce non-linear and

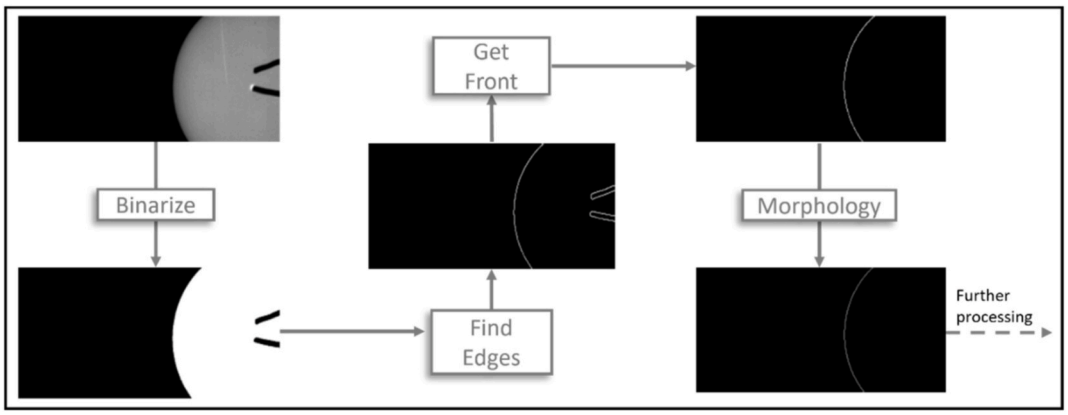

Fig. 3. Schematic of the front detection pipeline implemented in PropaTrack. The workflow includes image binarization, edge detection, and morphological refinement to isolate a clean reaction front for each frame.

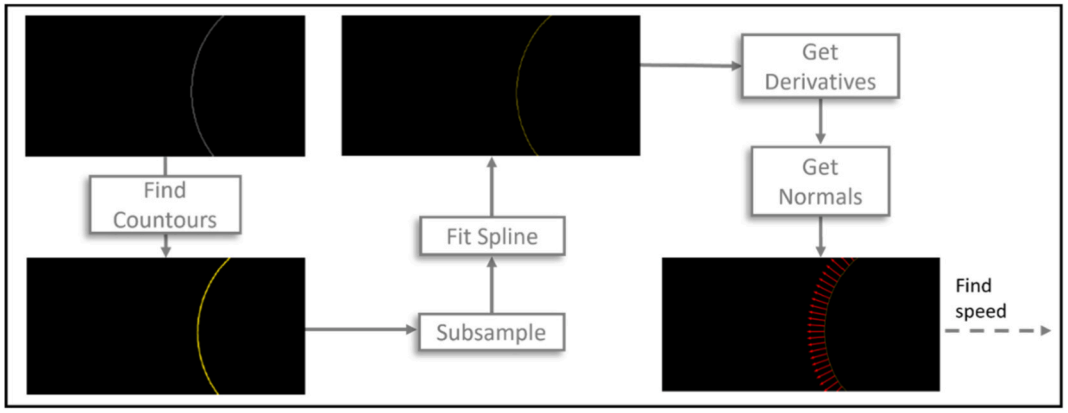

Fig. 4. Schematic of the velocity estimation workflow in PropaTrack. The detected front is subsampled, fitted with a spline, and used to compute local normal vectors. These are then compared across consecutive frames to extract local velocity vectors.

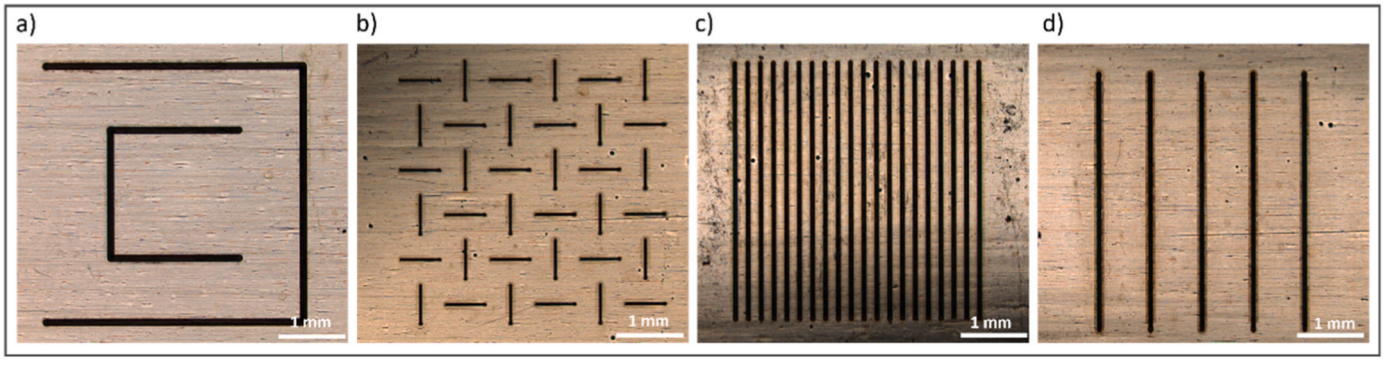

Fig. 5. CLSM micrographs of the four micromachined patterns: (a) Double C, (b) Maze, (c) VL-0.2, and (d) VL-0.8. Each pattern was structured over an area of 16 mm2, and all laser-cut trenches fully penetrated the 40 μm thick Ni/Al RMF.

discontinuous reaction paths, incorporating turns, enclosed regions, and detours. In contrast, the VL-0.2 and VL-0.8 maintain an overall linear geometry, but introduce periodic trenches perpendicular to the propagation direction, allowing a more controlled comparison of how periodic interruptions affect the reaction. These two structures are analyzed as a parametric pair to isolate the influence of line spacing on propagation dynamics.

Together, these geometries capture different mechanisms by which geometry can tailor reaction behavior: redirection, splitting and merging and periodic modulation. Their selection therefore enables both systematic and comparative evaluation across distinct design principles. Their well-defined geometry and reproducibility made them suitable for frame-by-frame velocity tracking and quantitative comparison. An unstructured reference samples (Standard) was included to serve as a baseline to represent uninterrupted planar propagation and enable direct comparison of how the structured patterns modify reaction behavior.

3.2. Reaction behavior from high-speed imaging

High speed imaging was used to assess how the reaction front evolves in the presence of laser-induced geometries. Each pattern provides a distinct mechanism of interaction with the advancing front, as captured in time-resolved frames. Due to the uniform and homogeneous propagation observed in the unstructured standard sample, still frames are omitted for brevity. The full reaction is available on Video S1, Supporting Information.

Supplementary video related to this article can be found at https://doi.org/10.1016/j.mtadv.2025.100648.

Selected top-view frames showing the reaction for the **Double C** pattern are shown in Fig. 6. The total reaction lasted approximately 2.27 msec, the longest among all samples. The full sequence is available on Video S2 (Supporting Information). As shown in Fig. 6b–e, the reaction front moves upward and enters the first C-shaped cut-out at around 1.37 msec. Upon entering the structure, the front immediately splits into two branches, propagating along the upper and lower arms of the larger C. These two branches advance independently and later converge at the center of the structure, forming a bright merging zone likely associated with localized heat accumulation. A similar split-merge sequence occurs at the smaller C. In this geometry, the front reaches the center of the inner C at around 2.08 msec (Fig. 6d), whereas in the unstructured foil it would reach the same position after only 1.1 msec. This shows the significant delay introduced by the Double C pattern, along with a redistribution of heat release over a longer time due to repeated splitting and merging events.

Supplementary video related to this article can be found at https://doi.org/10.1016/j.mtadv.2025.100648.

Fig. 7 shows the selected still frames of the **Maze** pattern. The full reaction can be seen on Video S3 (Supporting Information). The reaction lasted approximately 1.83 msec, longer than the standard (1.55 msec). Upon entering the Maze structure (Fig. 7b–d), the front encounters a staggered arrangement of vertical and horizontal trenches. Vertical trenches split the front into several branches that move through adjacent segments. In contrast, horizontal trenches cause minimal disturbance, allowing smoother propagation. As propagation continues, partial fronts gradually merge at junctions, forming bright convergence zones. The front becomes increasingly fragmented and dispersed, with an irregular morphology and a combination of splitting, confinement and merging.

Supplementary video related to this article can be found at https://doi.org/10.1016/j.mtadv.2025.100648.

Fig. 8 presents the corresponding still frames for the **VL-0.8** pattern. The full reaction can be seen on Video S4 (Supporting Information). The total reaction time was 1.85 msec, the second longest among the tested samples. In Fig. 8b–d, the reaction front experiences brief decelerations as it encounters each of the periodically spaced laser-cut trenches. At each trench, the front splits and travels along the edges of the vertical lines before merging at the center, producing a stair-like propagation profile. These periodic interruptions fragment the front, with a bright horizontal line forming along the centerline of the foil.

Supplementary video related to this article can be found at https://doi.org/10.1016/j.mtadv.2025.100648.

Fig. 9 presents the selected frames of the **VL-0.2** sample. The complete reaction is shown in Video S5, Supporting Information. The total reaction duration was approximately 1.80 msec. As shown in Fig. 9b–e, the front undergoes frequent interruptions when entering the structured region. It splits into multiple segments and propagates through alternating channels, similar to VL-0.8, but the narrower spacing increases confinement. This generates smaller thermally isolated zones, subtly changing the propagation dynamics. A distinct vertical bright line appears at the centerline, indicating repeated front merging. Compared to VL-0.8, the 0.6 mm reduction in trench spacing leads to more pronounced dynamics modulation. This is consistent with prior findings where reducing line spacing from 60 to 20 μm caused a 27 % reduction in front velocity [35]. These results reinforce how fine-tuned geometries can effectively control reaction propagation.

Supplementary video related to this article can be found at https://doi.org/10.1016/j.mtadv.2025.100648.

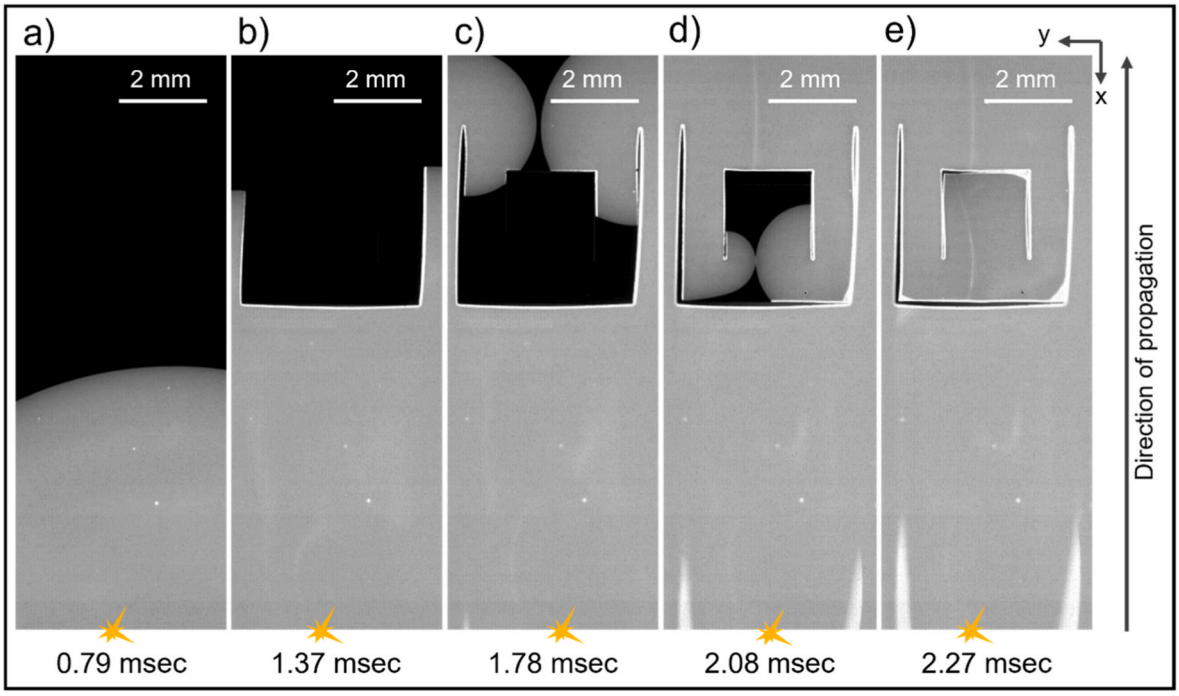

Fig. 6. Selected top-view frames of the Double C pattern: a) t = 0.79 msec, b) t = 1.37 msec, with the front propagating along the sides of the big C, c) merging point of the in the large C (t = 1.78 msec), d) merging point in the small C (t = 2.08 msec) and e) final frame after reaction completion (t = 2.27 msec). The yellow spark represents the ignition point, and the direction of propagation is from bottom to top.

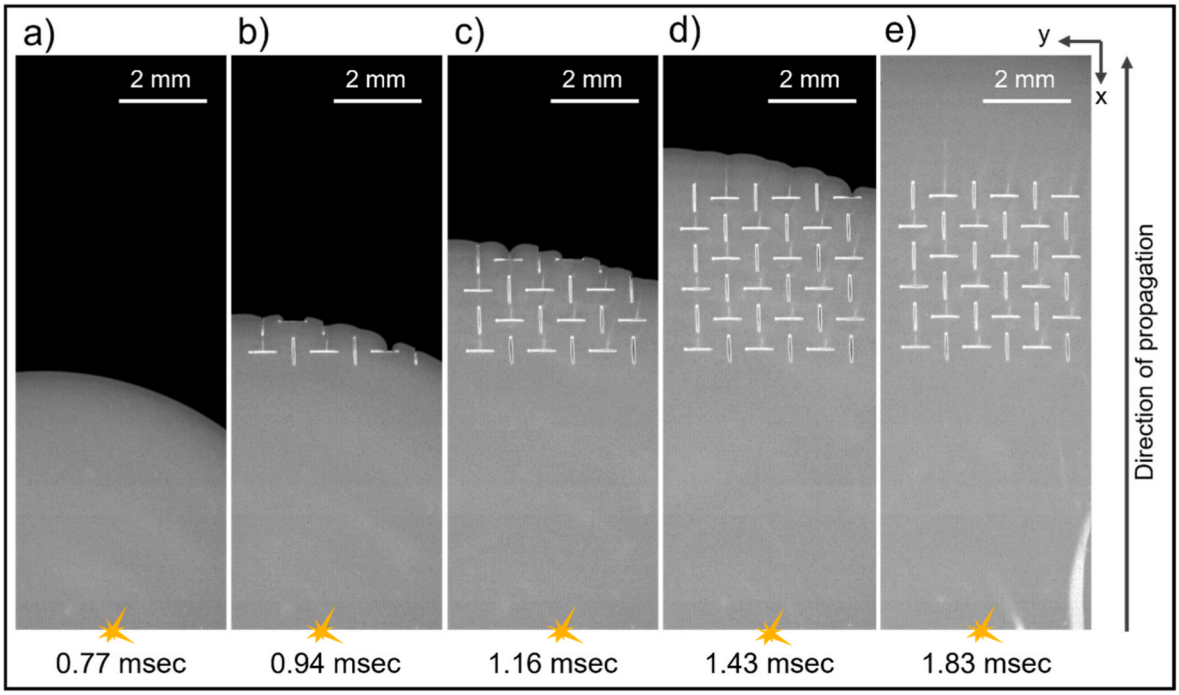

Fig. 7. Selected top-view frames of the Maze pattern: a) t = 0.77 msec, b) front entering the structure (t = 0.94 msec), c) front traveling around the vertical and horizontal trenches (t = 1.16 msec), d) exiting the structure (t = 1.43 msec) and e) final reaction frame (t = 1.83 msec). The yellow spark represents the ignition point, and the direction of propagation is from bottom to top.

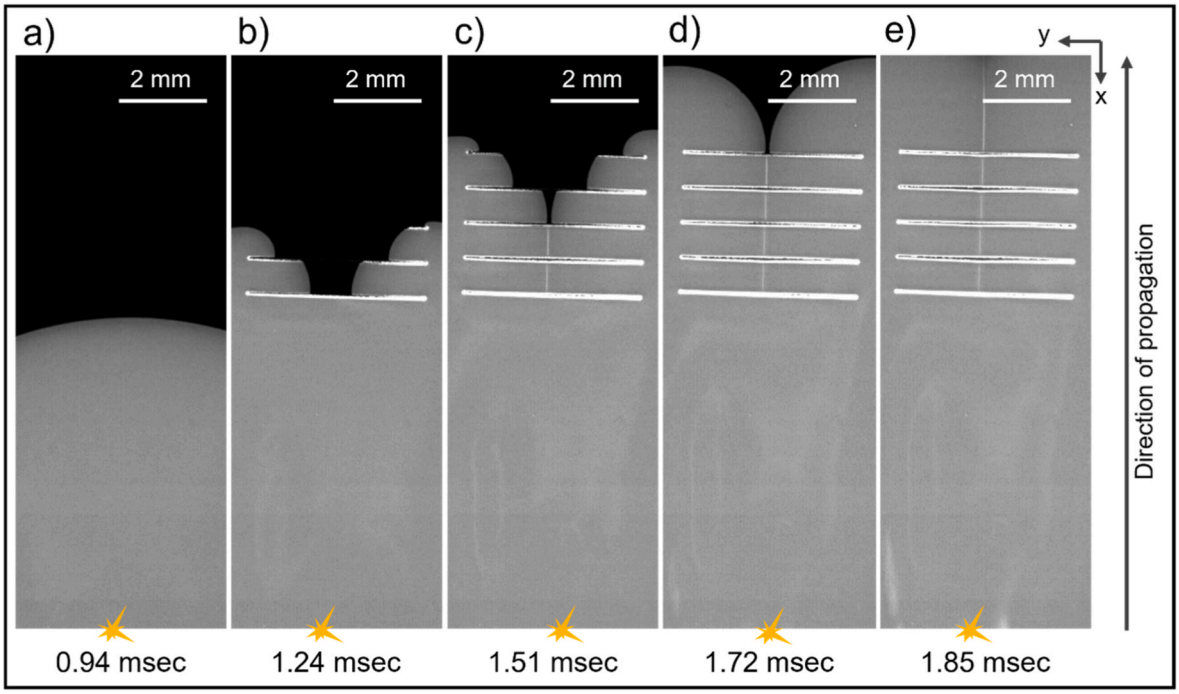

Fig. 8. Selected top-view frames of the VL-0.8 pattern: a) t = 0.94 msec, b) front propagating through the vertical lines (t = 1.24 msec), c) midpoint of structured region (t = 1.51 msec), d) exiting final trench (t = 1.72 msec), and e) reaction completion (t = 1.85 msec). The yellow spark represents the ignition point, and the direction of propagation is from bottom to top.

3.3. Validation of image analysis algorithm (PropaTrack)

To validate the accuracy of PropaTrack, a manual reference measurement was performed using ImageJ [49]. For each pattern, the same frames were analyzed with both methods. In ImageJ, the distance traveled by the reaction front in the region called merging zone was manually tracked and divided by the time interval. In PropaTrack, the velocity was extracted directly from the vector field at the same region. Table 1 summarizes the comparison, showing close agreement between both methods, with PropaTrack capturing slightly more localized variations.

The quality of the generated velocity fields was found to be

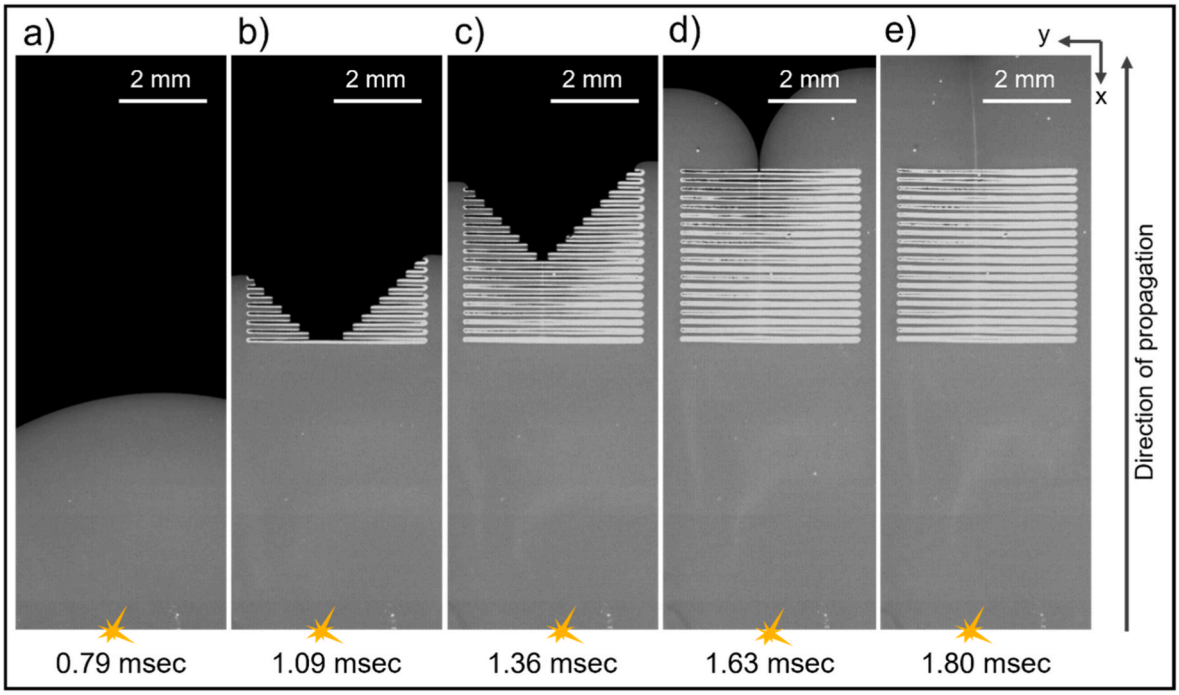

Fig. 9. Selected top-view frames of the VL-0.2 pattern: a) t = 0.79 msec, b) front navigating the densely spaced vertical lines (t = 1.09 msec, c) midpoint of structured region (t = 1.36 msec), d) final merge (t = 1.63 msec) and e) final frame after reaction completion (t = 1.80 msec). The yellow spark represents the ignition point, and the direction of propagation is from bottom to top.

Table 1
Comparison of reaction front velocities measured at the same region of structured Ni/Al multilayers using manual tracking (ImageJ) and PropaTrack (automated algorithm). The results confirm good agreement between both methods and validate the reliability of PropaTrack of local velocity extraction.

Patterns	Velocity PropaTrack (m/s)	Velocity ImageJ (m/s)
Double C (merge)	22.48 ± 2.3	24.12 ± 2.8
VL-0.2 (merge)	20.67 ± 1.1	19.83 ± 1.3
VL-0.8 (merge)	22.53 ± 3.4	21.10 ± 2.4

dependent on the spacing between laser-cut trenches. Vector fields remained interpretable for horizontal line spacings 90 μm or greater. However, when the spacing was reduced to 30 or 60 μm, the reaction front in the structured region became too fragmented for reliable vector generation, as seen in Fig. 10. These observations are based on recordings acquired with a different optical setup than that used for the main study. For the 30, 60 and 90 μm line spacing recordings, a Navitar 3x lens was used, providing a field of view of approximately 0.8 × 0.4 mm^2 at 210k fps, corresponding to a pixel size of 3.2 μm. Although this configuration yields more pixels across the narrow gaps (~19 pixels for 60 μm spacing) than in the Macro lens recordings of the 0.2 mm line spacing sample used in this work (Fig. 5c), which has approximately 10 pixels, segmentation quality was still poorer for the narrower Navitar recordings. This indicates that pixel density alone does not define the detection limit. Another contributing factor appears to be the lower image sharpness of the Navitar recordings compared to the Macro setup, which reduces effective edge detection. The reduced sharpness makes reaction front extraction more difficult, increasing the chances of fragmentation during binarization and contour extraction. The observed limitation is therefore a combined effect of optical resolution, image quality and the intrinsic morphology of the reaction front in narrow gaps. Analyzing smaller line spacings would require not only sufficient spatial resolution but also enhanced image sharpness and potential improvements to the front-detection algorithm.

3.4. Global reaction velocity

To evaluate how laser-induced micromachining affects the propagation dynamics of self-propagating reactions in Ni/Al multilayer foils, the reaction front velocity was extracted by frame-by-frame from high-speed video recordings. For each pattern and the unstructured reference sample (Standard), the local front velocity was measured using the PropaTrack image analysis algorithm, which enables high spatial and temporal resolution tracking across the entire reaction. To minimize noise introduced by image artifacts and end-of-reaction irregularities, only velocities measured within a 1 mm window before and after the structured region were included. This window isolates the pattern's influence while reducing variability from ignition and edge effects. Additionally, outliers were removed by thresholding velocities between 6 and 25 m/s for the structured samples and 6 and 10 m/s for the Standard. Furthermore, because for some samples the post-structure is shorter than the pre-structure interval, the number of data points in this region is limited, which can increase statistical uncertainty. Trends in this region are therefore interpreted cautiously.

Fig. 11 shows the normalized average per frame front velocity over time for the Double C and Maze patterns. To allow direct comparison, the Standard is plotted as a reference line (dotted black line). Time zero corresponds to the moment the front enters the 1 mm pre-structure interval, not ignition time. Velocities were normalized by the average measured during the pre-structure interval. Shaded regions mark the 1 mm pre- and post-structure, and the unshaded center corresponds to the structured zone. The Standard shows smaller scatter than the structured patterns and is therefore plotted as a black dotted line to make direct comparison easier. This allows the increased fluctuations in the Double C and Maze to be attributed to geometry-front interactions rather than measurement noise.

The Maze pattern shows a relatively stable velocity profile throughout the structured zone. Although the geometry forces the front through alternating vertical and horizontal channels (Fig. 7), the overall velocity remains near the pre-structure baseline. The front that consistently splits at vertical trenches and flows through horizontal ones, leads

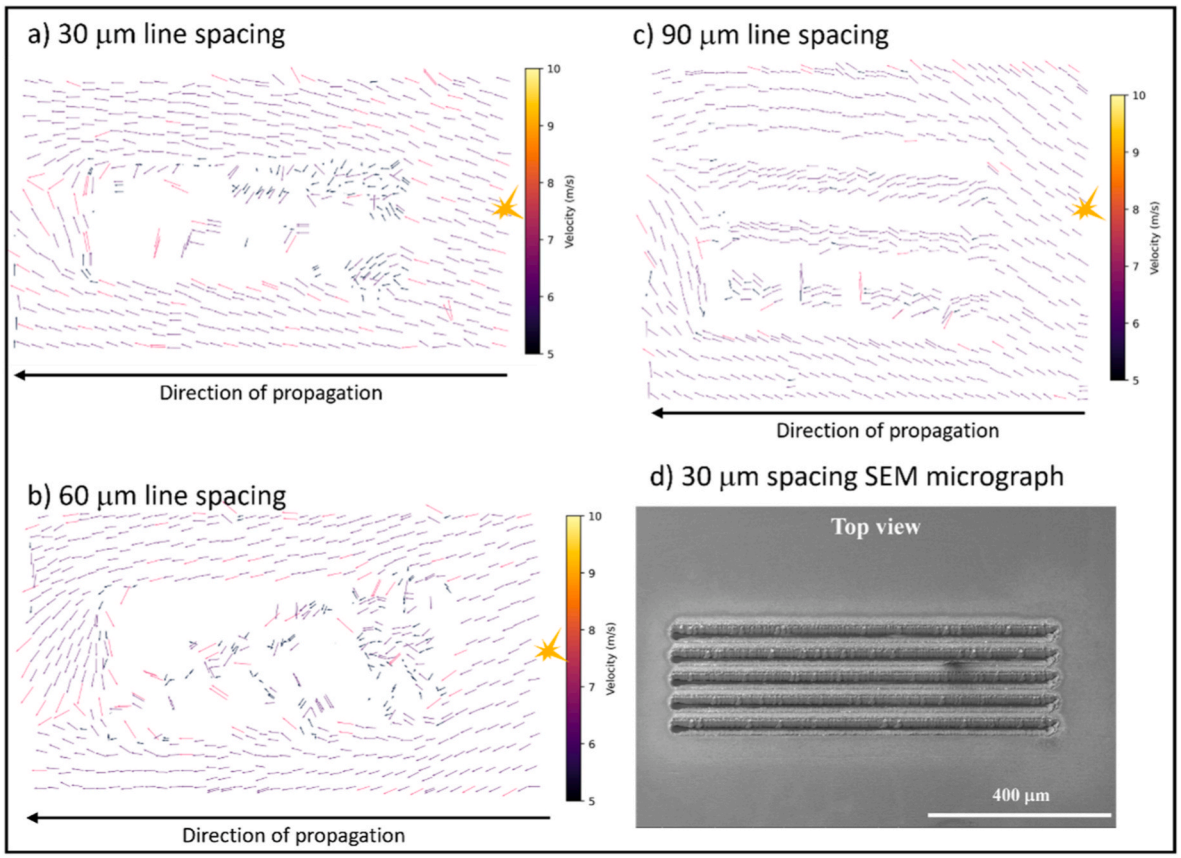

Fig. 10. Vector field comparison for structures with: a) 30 µm, b) 60 µm, c) 90 µm line spacing and d) 30 µm SEM micrograph of the horizontal line, illustrating the pattern appearance (only the spacing was varied across the three samples). As the spacing increases, the vector field becomes more reliable in the structured region. The yellow spark represents the ignition point. Field of view is 0.8 × 0.4 mm^2.

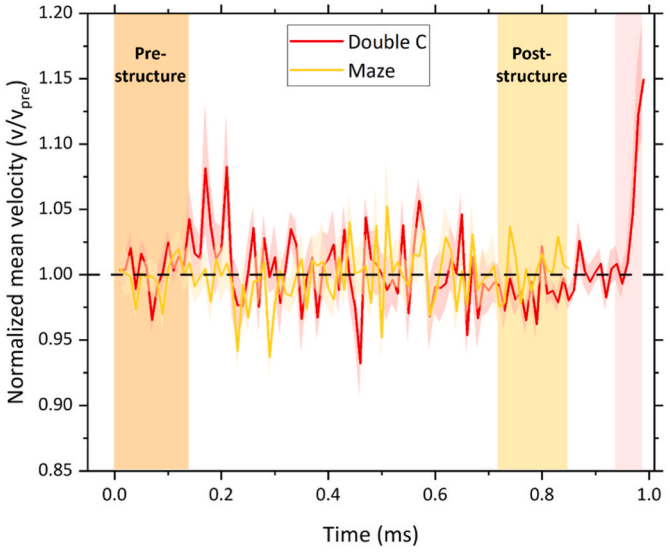

Fig. 11. Normalized average front velocity over time for the Standard sample (dashed black line), Double C pattern (red line), and Maze pattern (yellow line). Velocities are normalized to the pre-structure average. Left shaded block marks the pre-structure interval and the right shaded block the post-structure interval. The red shade rectangle corresponds to the intervals for the Double C and the yellow shades the intervals for the Maze. Time zero corresponds to the moment the front enters the 1 mm pre-structure measurement interval.

to a fragmented but still uniform propagation. Its velocity remains close to the Standard throughout the structured region, indicating that despite its geometric complexity, the global propagation rate is only mildly affected. The near-identical times required to travel the pre- and post-structure segments further support the interpretation that, while the front is geometrically redirected, its average velocity seems to remain stable.

In contrast, the Double C displays a more complex velocity profile, characterized by larger fluctuations in propagation speed. These oscillations reflect the front's dynamics response to the constant reorientation imposed by the C-shaped layout. Unlike the Maze, which maintains relatively stable propagation through a staggered propagation, the Double C creates localized convergence zones that concentrate thermal energy and induce velocity instabilities. A significant velocity peak appears in the 1 mm post-structure interval. Although this region lies outside the micromachined area, it coincides with the merging of the fronts exiting the large C. This convergence phenomenon produces localized acceleration causing the burst in velocity at this stage. It is important to note that the reaction within the smaller inner C remains active during this interval, adding further complexity to the measured profile. Due to its localized acceleration near the merging zones, the Double C front completes the 1 mm post-structure faster than the Maze, despite its overall longer reaction time, while pre-structure times remain equivalent, confirming comparable behavior in unstructured regions.

Fig. 12 shows the normalized average velocity profiles for VL-0.8 and VL-0.2 patterns, both featuring vertically aligned trenches with identical geometry but different line spacing. Again, velocities were normalized to the pre-structure average, with shaded regions marking pre- and post-structure intervals.

The VL-0.8 shows mild oscillations across the structured region, with

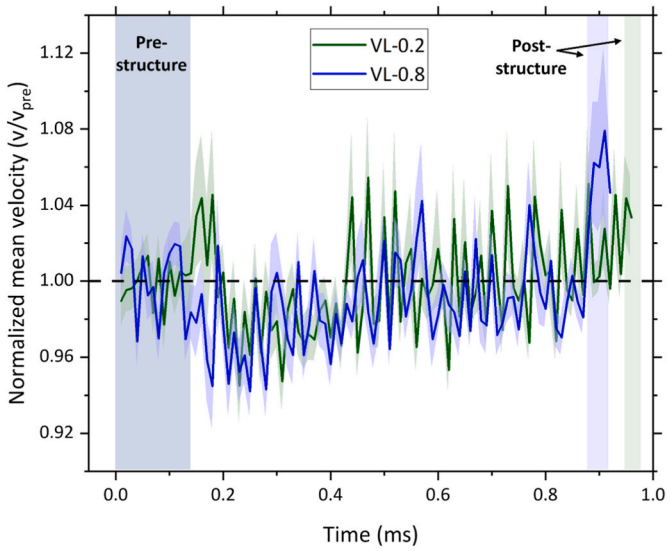

Fig. 12. Normalized global front velocity over time for the Standard sample (dashed black line), VL-0.8 (blue line), and VL-0.2 pattern (green line). Shaded regions indicate the 1 mm pre- and post-structure intervals. Upon entering the structuring, VL-0.8 shows a transient velocity drop. In contrast,VL-0.2 exhibits a brief initial rise followed by a drop, mirroring VL-0.8's behavior until mid-structure, after which VL-0.2 velocity increases again. These differences in velocity modulation reflect the impact of trench spacing on front dynamics.

lower amplitude fluctuations than VL-0.2. A small velocity drop occurs almost immediately after entering the structured zone, likely due to brief slowdowns when the front crosses the first trench and continuity is temporarily disrupted. Similar short interruptions occur at later trench crossings, keeping the velocity slightly below the Standard in some segments. Apart from these short interruptions, no pronounced local accelerations were observed. Furthermore, a subtle velocity increase appears near the post-structure merging zone, similar in nature, but smaller in magnitude, to the behavior observed in the Double C.

In contrast, the VL-0.2 shows a more dynamic behavior with higher velocity variations from the baseline. At the entrance of the structured region, it exhibits initial acceleration, in contrast to the drop seen in VL-0.8. This might result from the denser trench spacing, which causes earlier interactions between closely spaced split segments, allowing multiple propagation paths to form quickly. Shortly after the initial acceleration, VL-0.2 also shows a velocity drop, and from that point onward, both patterns follow similar behavior until the middle of the structured interval, with velocities remaining below the Standard in several segments. The dense trench arrangement forces the front to split more frequently, with multiple narrow segments propagating in parallel. The average velocity profile shows peaks and dips within the structured region, which likely arise from the complex interaction between repeated splitting, merging and other reorganization processes as the front travels through the dense trench pattern. VL-0.2 achieves peak velocities higher than VL-0.8, and although it also dips below the Standard, its average velocity across the structure is higher. Pre-structure speeds are comparable for both, but VL-0.2 completes the post-structure interval slightly faster. This suggests that closer trench spacing promotes stronger temporal and spatial variations, leading to a more uneven but overall faster propagation through the structured region.

Table 2 summarizes the average global velocity, the pre-structure velocity and total reaction time for all patterns and the Standard. These metrics complement the time-resolved profiles and characterize full propagation behavior. Across the samples, the pre-structure velocities closely align with their respective global averages, suggesting that the global metric is largely influenced by unstructured regions. This dominance can mask geometry-specific effects, which are more accurately captured through local, frame-by-frame analysis presented in the next section (Section 3.5). The Standard sample has the lowest average speed and shortest reaction time of all samples, establishing the baseline performance for unmodified commercial Ni/Al foils. Double C has the highest velocity but longest duration, reflecting complex merging dynamics. VL-0.2 achieves high velocity and short reaction time. Maze and VL-0.8 display moderate speeds and durations, confirming their smoother impact.

Table 2
Average global reaction velocity, pre-structure velocity and total reaction time each structured pattern and the unstructured Standard sample. The standard sample shows both the lowest average speed and the shortest total reaction time among all samples. This reflects its homogeneous, unstructured propagation path. Pre-structure values are taken from the unstructured window immediately before the front reaches the laser-cut patterns.

	Standard	Double C	Maze	VL-0.2	VL-0.8
Average global velocity (m/s)	8.71 ± 0.01	9.28 ± 0.01	9.02 ± 0.01	9.22 ± 0.02	9.03 ± 0.01
Pre-structure velocity (m/s)	–	9.24 ± 0.01	9.02 ± 0.02	9.20 ± 0.01	9.03 ± 0.02
Reaction total time (msec)	1.55	2.27	1.83	1.80	1.85

To assess how different patterns influence the complexity of the reaction front, the total reaction path length was computed as the frame-by-frame sum of the local displacements of all active front pixels extracted from the image analysis algorithm (Fig. 13). By definition, this metric scales with the instantaneous interface length and lateral deviations, not with the geometric start-to-end distance. The PropaTrack algorithm provides velocity magnitudes (in pixels per frame), which were first filtered to remove unrealistic values from segmentation noise or artifacts. These values were then converted to real units using the calibrated scale of 1 pixel = 0.0201 mm. The resulting path-length values reflect how structuring causes the front to deviate from a planar trajectory. For additional comparison, the total path length was normalized by the total path length of the Standard foil to obtain a dimensionless relative path extension ratio.

Among the structured samples, VL-0.2 shows the largest path extension, with a 20 % increase over the Standard, reflecting an extensive redirection imposed by its dense trench spacing. Although longer trajectories are typically expected to result in longer reaction times, VL-0.2 combines the longest path with the shortest total duration among the structured (Table 2). This indicates that the geometry enables efficient

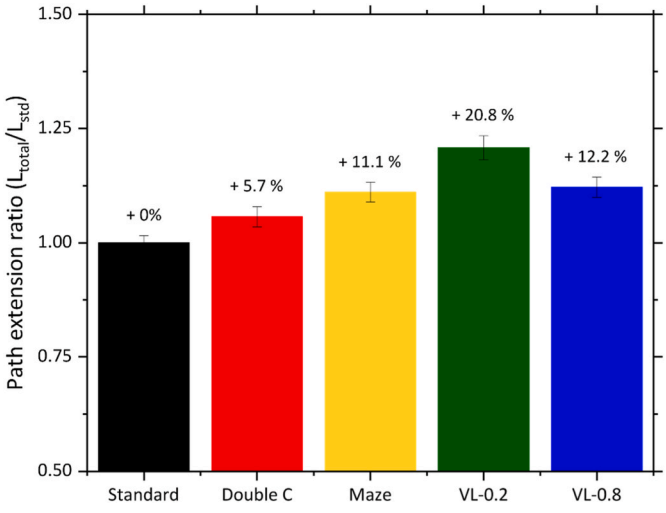

Fig. 13. Normalized reaction path length for all samples. Patterns induce different degrees of front redirection, with VL-0.2 producing the most extended path with a 20.8 % increase compared to Standard.

redirection without significant interruption, allowing the front to travel farther without requiring additional time. In contrast, the Double C pattern results in the shortest path among the structured geometries but the longest total reaction time. This indicates a different kind of geometric influence: the structure delays the front not by increasing the distance traveled, but by fragmenting the propagation into distinct stages, due to its complex layout and splitting/merging behavior. Thus, the extended propagation time in Double C is not linked to how far the front travels, but to how and when the front moves.

The Maze and VL-0.8 patterns fall between these extremes and display similar behavior to each other. Both produce longer paths than Double C, have lower average velocities than Double C and VL-0.2, and require slightly more time to complete the reaction than VL-0.2. Maze likely achieves this via uninterrupted lateral propagation, which allows for continuous propagation without sharp reorientation. VL-0.8, by contrast, extends the path moderately, not due to intense redirection like the VL-0.2, but due to its simpler geometry allowing the front to meander more gently. This increased the total path length, though not to the same extent as VL-0.2, which still shows a 9 % longer path due to the stronger and more frequent redirection. Thus, VL-0.8 results in a considerably long trajectory for a less complex structure.

Together, these results show that laser structuring tailors reaction propagation not only in velocity, but also in how the front evolves across space and time. VL-0.2 achieves fast, redirected propagation, Double C imposes delays due to its complex geometry that enables multiple front-splitting events and subsequent thermal convergence zones. Maze and VL-0.8 offer mild modulation without dramatic changes. All micromachined patterns achieve higher total average velocities, longer paths and reaction time than the Standard, showing how geometric modifications can modulate the self-propagating reactions in Ni/Al multilayers. These observations are consistent with recent studies demonstrating that structural features such as engineered surface patterns or even defects like cracks can influence the propagation behavior of self-propagating reactions in multilayer systems [41,50].

3.5. Local reaction velocity

While average velocities provide a useful overview of global propagation trends, they can mask important local variations that happen during the reaction. These local effects, such as directional changes, front splitting and merging, and transient accelerations, can play a role in defining the thermal and kinetic behavior of the system. To better capture these effects, this section focuses on the full spatial and temporal resolution of the velocity data already extracted using the PropaTrack image analysis. Instead of averaging across the reaction front, local velocities at each pixel row and frame are treated as individual data points. This enables a more detailed view of how the front responds to specific geometrical features. By examining the distribution and evolution of these local velocities, it becomes possible to distinguish between uniform and heterogeneous front dynamics and explore localized phenomena that are otherwise hidden in averaged plots.

Although temperature measurements are not included in this study, prior work has demonstrated a strong correlation between local reaction velocity and thermal output in reactive multilayer systems [51]. A study showed that in Al/Monel multilayers, premixing during deposition significantly lowers the heat of reaction and final temperature, leading to reduced propagation velocity. In Ni/Al multilayers, similar effects occur at small bilayer periods, where premixing can reduce the final temperature below the melting point of NiAl and slow the reaction down [52]. Additionally, another study showed that increasing the thickness of the intermixed region significantly reduces the heat of reaction and maximum temperature, leading to a sharp decrease in propagation velocity, especially for bilayer thicknesses below 25 nm [53]. Velocity bursts, where the front momentarily accelerates, are typically linked to rapid energy release and elevated temperatures. For example, alloying Ni/Al multilayers with copper reduced the front temperature by 800 °C and slowed the velocity to 0.6 m/s, while platinum alloying increased the temperature by 800 °C and raised the velocity to over 40 m/s [54]. These results are consistent with the idea that higher thermal intensity can be associated with faster propagation, although changes in RMF chemistry also influence reaction kinetics. This interpretation is supported by the appearance of the bright lines observed during high-speed imaging, which coincide with the fastest regions of the front, suggesting heat accumulation at merging zones.

In contrast, several studies have shown that passive substrates or interfacial obstacles can reduce both reaction velocity and temperature due to enhanced heat dissipation into surrounding materials [35,38,39]. These effects are particularly prominent in supported foil configurations where the substrate act as a heat sink. However, the present observations involve free-standing foils with internal geometrical structuring, eliminating substrate-induced thermal losses while maintaining the benefits of geometrical control.

Although previous work has shown that oxide layers formed during femtosecond micromachining can also act as localized thermal barriers and reduce reaction velocity when the oxide-to-foil ratio is high (line spacings below 60 μm) [35], the smallest spacing between laser trenches in the present study is 200 μm. At this scale, the oxide proportion is small relative to the remaining foil, and oxide-related heat sinks effects are expected to be minimal. The observed differences in local velocity therefore suggest that geometric features, rather than oxide variability, are the dominant factor influencing thermal concentration and front dynamics. This interpretation is further supported by recent findings showing that substrate-free environments allow more pronounced local thermal effects [55], reinforcing the role of internal geometry in modulating reaction dynamics.

3.5.1. Double C pattern

The Double C provides a clear example of how laser-defined geometrical constraints locally influence the behavior and propagation of the reaction front. Fig. 14 presents the local velocity field for each frame during propagation through before and after the structured region. Each vector arrow indicates both the direction and magnitude of the local front velocity. Arrow length and thickness are related to speed, while the color map provides a complementary quantitative scale from 6 to 25 m/s and both correspond to the local speed, revealing spatially heterogeneous behavior throughout the structure.

The thicker and brightest arrows, corresponding to the highest local velocities, are concentrated in the central merging regions of both inner and outer C structures. These zones mark points where multiple fronts converge into a single reaction channel, leading to short but intense acceleration with velocity bursts approaching the upper limit of 25 m/s. In contrast, the arms and outer regions of the structure show more uniform and moderate propagation, typically ranging from 9 to 12 m/s, reflecting steady front propagation along unconstrained paths. The flow direction also adapts to the geometric curvature, particularly near corners and junctions, indicating that both speed and angular orientation are being shaped by the structure. These events are not random fluctuations but are geometrically induced and repeatable.

These observations are reinforced by the velocity distribution shown in Fig. 14b. The histogram shows the spread of local velocities across the region seen in the velocity field for the Double C, with the Standard included for comparison. Relative to the Standard, the Double C shows a broader distribution with a more pronounced tail toward higher velocities. This indicates that the Double C geometry does not only speed up the front in a global manner but also introduces high-frequency local bursts in specific regions, effectively shaping the reaction. These high-velocity regions are interpreted as localized bursts of energy delivery, consistent with the merging-induced acceleration and the bright emission lines visible during the reaction.

This ability to spatially program regions of high local velocity could have direct implications for bonding applications and localized thermal processing. In the Double C pattern, merging fronts produced localized

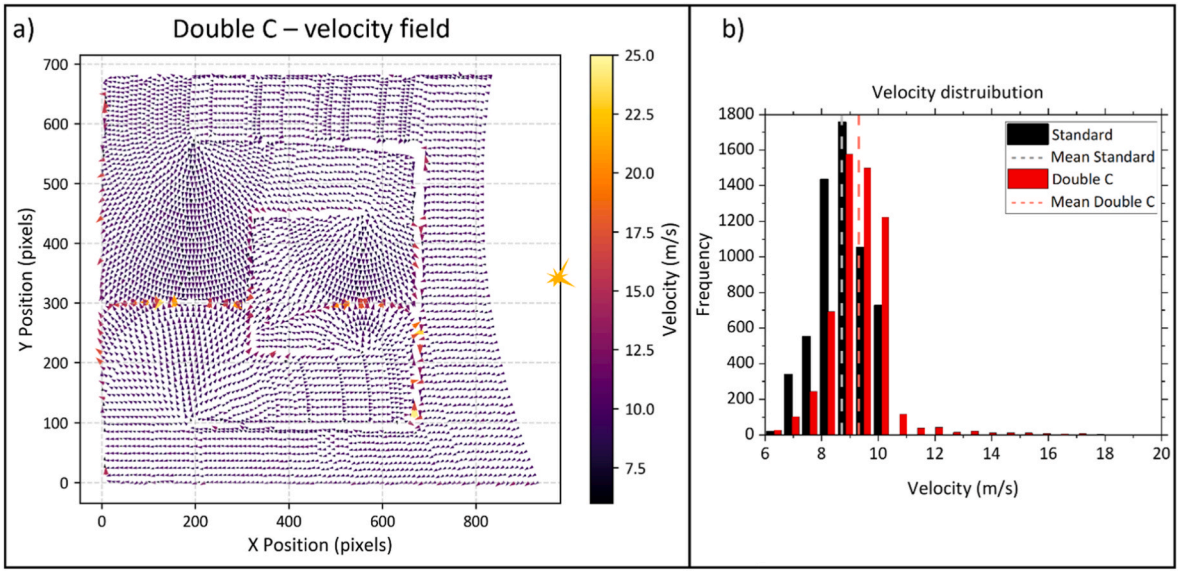

Fig. 14. a) Local velocity field of the Double C pattern extracted from the image analysis algorithm. Arrows indicate direction of propagation, with color and thickness representing velocity intensity. The highest velocity vectors (~25 m/s) are localized at merging zones, particularly where converging fronts intersect. b) corresponding velocity distribution histogram for the same region analyzed in the velocity field for the Double C, with the Standard histogram included for comparison. The dashed lines represent the corresponding mean velocity. The Double C distribution shows a strong peak near the average but also a trail towards higher velocities, indicating the presence of short bursts of fast propagation that elevate the mean velocity and show how the Double C promotes localized velocity enhancement through structural complexity.

acceleration zones, while adjacent regions maintain lower velocities. This combination shows how femtosecond laser structuring can be used not only to guide reaction pathways, but also to modulate the spatial and temporal distribution of energy during self-propagating reactions.

3.5.2. *Maze pattern*

The Maze pattern was designed to challenge the propagation front with a highly complex geometrical architecture, where multiple narrow channels would force the reaction to repeatedly split, reorient, and travel through different paths. As shown in Fig. 15a, the local velocity field reveals a complex mosaic of directional changes, segmented flow, and constrained accelerations. While most arrows fall in the 8–12 m/s range, localized bursts approaching 25 m/s appear at convergence zones.

Unlike the Double C, which concentrates acceleration into two dominant convergence zones, the Maze distributes high-velocity events periodically along the path. These bursts are visually identifiable as thicker and brighter arrows aligned with the vertical channels in the structure, suggesting that the pattern functions as a periodic velocity modulator, reflecting a more fragmented, decentralized type of energy delivery. Additionally, some vectors near convergence zones deviate slightly from the main flow, indicating very local and small backflow or redirection, further emphasizing the complexity induced by the Maze geometry.

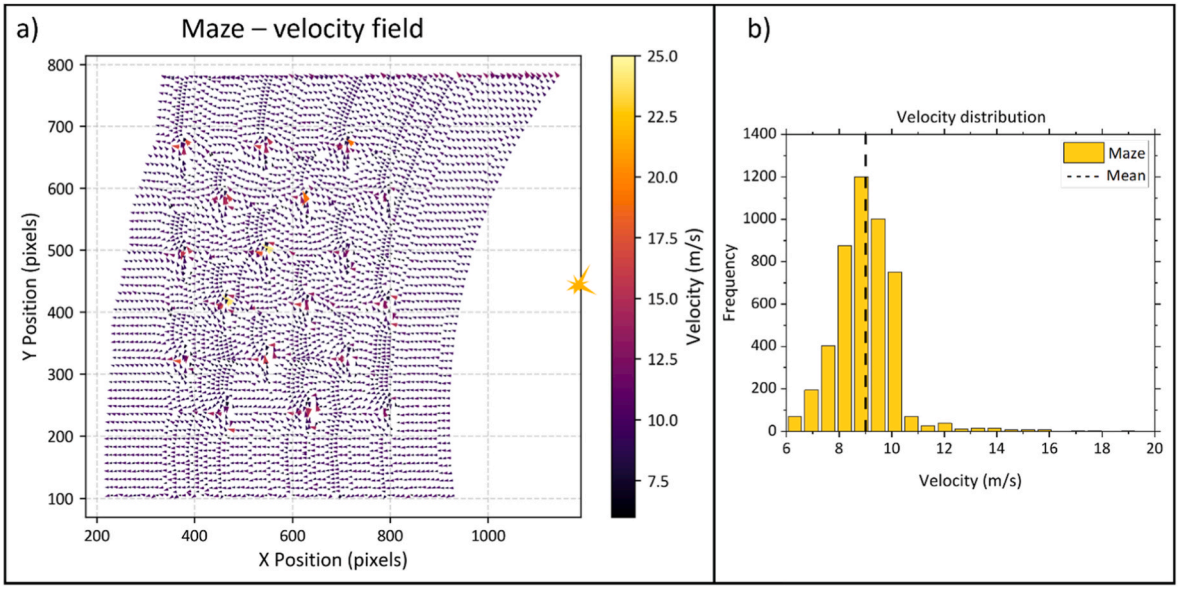

Fig. 15. a) local velocity field for the Maze pattern. Localized velocity bursts appear along vertical corridors and sharp turns, where the front is redirected or merges from opposing fronts. b) corresponding histogram showing a narrow and more symmetric distribution centered around 9 m/s. The small high-velocity tail shows that brief acceleration happens, but overall, the propagation remains smooth.

The corresponding velocity distribution in Fig. 15b reflects this behavior. The histogram is narrower and more symmetric than in the Double C (Fig. 14b), with a mean velocity centered at approximately 9 m/s. This supports the interpretation that the Maze pattern maintains a smooth propagation profile while still introducing localized accelerations at determined points.

The total reaction duration reflects the influence of its elongated, segmented path and frequent directional changes, which increase the effective distance traveled by the front, as seen in Table 2. As a result, Maze combines moderate overall velocity with structural complexity that shapes both the spatial distribution of localized heat bursts and the total time over which energy is delivered, offering a unique type of reaction control.

The Maze thus shows the potential to precisely tailor the spatial-temporal energy release. Unlike the Standard foil, which delivers heat uniformly, the Maze introduces localized bursts in specific regions without interrupting the front's propagation continuity. These observations indicate that the Maze can spatially vary the reaction front velocity, which may influence how and where energy is released during the reaction.

3.5.3. *Vertical lines with 0.8 mm line spacing (VL-0.8) pattern*

The VL-0.8 pattern introduces vertical channels at relatively wide spacing (0.8 mm). As shown in Fig. 16a, the velocity field shows that the front remains mostly forward directed, with minimal angular deviation. Most velocity vectors fall within a narrow range around 9–10 m/s, but localized accelerations appear where opposing fronts converge after entering the vertical lines channels from top and bottom. A final velocity burst is also observed at the final merging region.

An interesting observation is that the upper half of the structure, where the front enters the vertical lines from above, shows slightly more angular deviation and denser vector clustering than the lower half, which propagates more directly. This asymmetry is unlikely to originate from the pattern geometry, as the structure is symmetric and similar behavior is not observed in the VL-0.2 pattern, which shares the same configuration but with denser line spacing. High-speed video reveals that in both cases, the front initiates propagation slightly earlier from the bottom. Additionally, small variations in ignition position or filament contact may contribute to the observed asymmetry, highlighting how subtle experimental factors can influence front dynamics in reactive foils. Despite these variations, the merging in VL-0.8 happens precisely at the center of the structured region, suggesting that the VL-0.8 pattern appears to compensate for ignition offset through its structural configuration, guiding the fronts toward a balanced convergence.

These transient accelerations are visible as isolated bright arrows within the structured region and the velocity bursts appear both at the merging zone inside the vertical lines and at the final convergence point, similar to the behavior observed in the Double C. However, in VL-0.8 these bursts are less intense, contributing to a narrower overall velocity distribution. The corresponding histogram in Fig. 16b reflects this balance, it shows a sharp peak around 9 m/s, with a low intensity trail extending toward higher values. This distribution is like the one seen in Maze pattern, which also combines moderate baseline velocities with localized bursts. However, while the Maze produces small and repeated redirection and distributed flow splitting, the VL-0.8 structure channels the front through discrete vertical gaps, resulting in more uniform flow and reduced angular complexity.

3.5.4. *Vertical lines with 0.2 mm line spacing (VL-0.2) pattern*

Fig. 17a shows the local velocity fields for VL-0.2 pattern and reveals a distinctly different behavior compared to the wider VL-0.8 pattern. Upon entering the vertical line channels from the top and bottom, the reaction front reorients sharply, propagating nearly orthogonally along the line axis. A particular feature of VL-0.2 is the pronounced velocity bursts that occur inside the lines, where fronts entering from opposite directions converge. These high-velocity regions appear as bright, thick arrows aligned along the central region of the structure and are more intense than those observed in VL-0.8. A final acceleration is again observed at the last merging zone. This more intense local acceleration is also reflected in the velocity distribution shown in Fig. 17b. The histogram reveals a broader spread and higher velocity tail than in VL-0.8, with peaks exceeding those observed in the Double C pattern.

These results suggest that despite its narrower spacing, the VL-0.2 significantly increases the frequency and intensity of localized bursts compared to VL-0.8. This higher density or bursts concentrates energy release into short time intervals and confined regions, contributing to the faster overall reaction time observed.

The spatially resolved velocity fields analyzed in this section reveal that geometrical patterning governs not only the direction of front propagation but also spatial distribution. These local dynamics, which

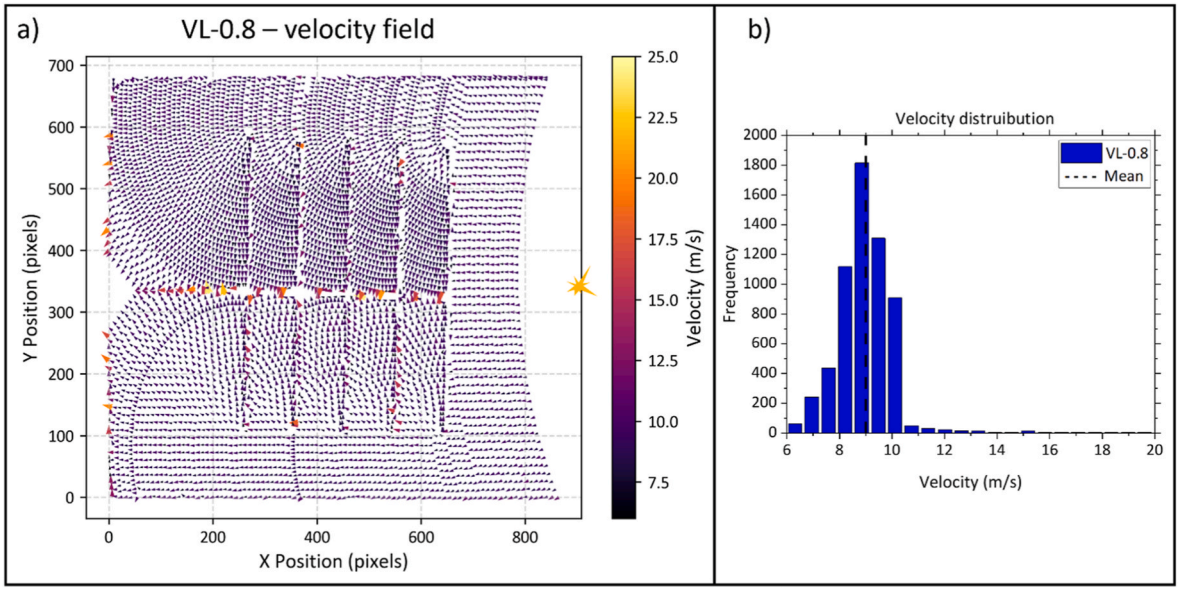

Fig. 16. a) local velocity field for VL-0.8, showing a uniform forward propagation with modest velocity bursts at the interfaces where the front converges after entering each vertical channel and at final merging zone. b) histogram distribution with most values clustered between 9 and 10 m/s. The narrow symmetric distribution shows steady propagation, with a subtle tail extending toward higher values due to localized acceleration zones.

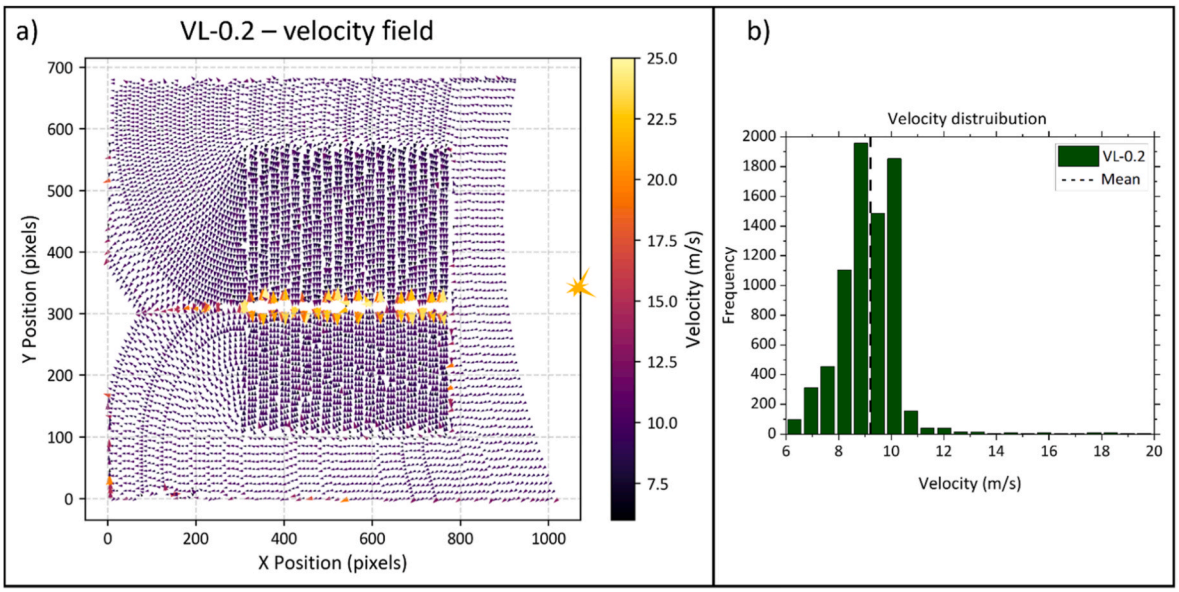

Fig. 17. a) local velocity field for VL-0.2, showing strong acceleration zones as the reaction front travels perpendicularly within narrower vertical lines. Similar to VL-0.8, velocity bursts appear where opposing front merge inside the channels and at the final convergence zone, though with greater intensity. b) histogram showing a broader distribution than VL-0.8, with pronounced tail toward higher velocities. The increased frequency of localized bursts contributes to a higher average velocity.

are not captured by average velocity profiles, are not random fluctuations but systematically induced by structural features such as merging zones, sharp redirection points, and confined propagation paths. The ability to manipulate these conditions through laser patterning enables a new form of thermal control that is tunable by design.

The comparison across patterns illustrates how geometry influences the behavior of the reaction. Double C and VL-0.2 produce frequent and spatially concentrated velocity bursts, driven by repeated front convergence and redirection. These patterns enable strong local acceleration and heat intensification, traits particularly suited for bonding processes that require sharp thermal spikes in specific regions. In contrast, Maze and VL-0.8 promote smoother propagation while still exhibiting localized bursts. These designs extend reaction times and increase global velocities relative to the unstructured foil, while maintaining a more gradual thermal profile, ideal for processes demanding controlled, distributed heating.

The differences between global trends (Section 3.4) and local trend behavior show the limitations of average metrics in complex structured systems. For example, Double C's highest average velocity coexists with the longest reaction time due to localized bursts that increase speed without accelerating the entire front. In VL-0.2's, the compact and frequent acceleration zones observed in the structured region may contribute to its faster overall propagation. This analysis demonstrates that prolonged reaction times arise from a combination of extended path length, temporary energy confinement at merging zones, and localized velocity reductions, and therefore velocity must be interpreted not only in terms of how fast the front propagates overall but also in the context of where, when and how energy is released.

The present results show that geometrical patterning alone can induce localized modulation of reaction front velocity and heat release. This reinforces the critical role of structural design in controlling reactive behavior and highlights geometry as an independent tuning parameter alongside composition. Similar to how internal structural modulation via inert CoAl interlayers in Co/Al multilayers has been shown to destabilize planar fronts and induce spin-like instabilities through internal structural modulation [56], the geometrical features introduced here act as engineered obstacles that reshape front trajectory and energy delivery profiles in predictable and designable ways.

The localized acceleration zones observed at merging fronts indicate transient regions of enhanced thermal release. In commercial Ni/Al multilayers, the reaction front temperature typically stabilizes near the NiAl melt isotherm [52]. However, the present results suggest that geometrically induced front merging may create local conditions that might favor increased energy release, producing brief velocity bursts. This behavior resembles the mechanism predicted for Co/Al multilayers [57], where colliding spin bands initiated forward propagation in otherwise non-propagating regions through localized heating above the product melt isotherm. Although temperature was not directly measured in the present study, as stated earlier, the spatial correlation between velocity bursts and bright emission zones supports the interpretation of transient thermal intensification. The experimental data presented here demonstrate that local velocities at merging zones exceed the pre-structure baseline, indicating that the engineered geometry promotes localized acceleration, potentially associated with short-lived increases in reaction temperature. These findings suggest that controlled front interactions can temporarily enhance the local reactivity of the multilayer, offering a new approach to spatially modulate heat release. Further studies involving direct temperature measurements are needed to clarify whether these localized bursts may transiently exceed the typical melt isotherm limit reported for Ni/Al systems.

3.6. Angular deviation and directional tailoring

To better understand the impact of laser micromachining on reaction dynamics, an angular analysis was conducted to measure the angular deviation of the reaction front from its primary propagation direction. While previous sections focused on velocity, reaction duration and path length, this analysis captures how pattern-induced deflections change the orientation of the propagating front at each point in space and time. Angular values were derived from the directional components of the local velocity vectors extracted using the image analysis algorithm. Specifically, the angle between each vector and the nominal propagation direction (right to left in the video frame) was calculated using the arctangent function and mapped to a range from 0° to 180°, where 0° corresponds to perfectly straight propagation, 90° to orthogonal and 180° to reverse motion. To ensure reliable analysis, only velocity vectors within the range of 6–10 m/s for the Standard foil and 6–25 m/s for structured samples were considered, minimizing the impact of noise and

artifacts same way it was done for the previous analysis.

To quantify directional deviations introduced by patterning, the angles calculated from the filtered velocity vectors were grouped into four angular bins: 0–45°, 45–90°, 90–135° and 135–180°. As shown in Fig. 18, the Standard sample displays a strong peak in the 0–45° range, with nearly all vectors aligned with the main propagation direction. All structured patterns also show their highest angular count in the 0–45° bin, which is expected given that a significant portion of the reaction happens in relatively straight propagation. However, compared to the Standard, the structured samples show broader angular distributions. Both Vertical Line configuration (VL-0.2 and VL-0.8) show increased occurrence in the 45–90° and 90–135° ranges, consistent with periodic redirection caused by splitting and merging around the vertical lines. The Double C is the only pattern exhibiting a significant amount in the 135–180° range, indicating local backward propagation that occurs as the reaction front enters and redirects within the arms of the smaller C structure. This demonstrates that angular deviation is not solely imposed by the trench geometry but also reflects dynamic effects such as merging and redirection.

The results demonstrate that angular deviation can be quantified and mapped frame-by-frame using the image analysis workflow. Structured patterns were found to increase both the frequency and spatial clustering of moderate-to-high angular deflections, particularly near turning and merging zones.

This behavior aligns with findings from previous studies on reactive multilayers featuring compositional or structural modifications. For example, one study demonstrated that substrate-induced structural features in Ni/Si multilayers can lead to non-uniform front propagation and angular deflections, showing how even subtle geometric variations can redirect energy flow and change local reaction dynamics [58]. Recent work further showed that externally induced cracks in Ni/Al multilayers can redirect the reaction front along meandering paths, modifying propagation velocity without affecting phase formation [41]. Additionally, another work revealed that periodic 2D surface structuring of substrates can systematically modulate propagation velocity and heat release by introducing growth defects that redirect the front [37]. Together, these studies reinforce the idea that angular propagation behavior is a powerful and tunable parameter in reactive system design, whether induced by compositional changes, substrate effects, or as demonstrated in this work, through deliberate geometrical structuring.

4. Conclusions

This study demonstrates that femtosecond laser micromachining of Ni/Al reactive multilayer foils enables effective tailoring of self-propagating reaction dynamics through geometrical patterning. By introducing distinct geometrical designs, it was possible to manipulate not only the reaction front's trajectory but also its local velocity, directional behavior, and energy distribution.

All structured samples exhibited longer reaction duration and greater traveled distances compared to the unstructured standard foil, with localized velocity bursts consistently occurring at merging and redirection zones. These bursts, captured through high-resolution image analysis, appeared to play a role in shaping both local heat release and global velocity trends. The Double C pattern emerged as one of the most effective designs, combining high global average velocity and strong localized acceleration with prolonged reactivity. The VL-0.2 pattern also produced local acceleration and higher average velocity than VL-0.8, indicating that even modest changes in design can substantially influence the front's behavior. Maze, while more moderate, also modulated the reaction, suggesting that mild but repeated redirection may be beneficial for smooth yet non-uniform thermal delivery.

By analyzing the reaction at high spatial and temporal resolution, frame-by-frame and vector-by-vector, this study reveals not only how different patterns affect reaction behavior but also where these changes happen. This level of detail provides a deeper understanding of the geometry-response relationship, supporting the possibility of programming the spatial and temporal characteristics of heat delivery. The frame-by-frame tracking capability enabled by the image analysis algorithm provided the resolution needed to quantify local acceleration zones and angular deviations, features that would remain hidden in conventional 'average-based' approaches. Although this study focused on free-standing foils and their fundamental behavior, the results suggest that structured multilayers can be used to design tailored heat profiles for bonding and joining processes, particularly in applications where precise thermal management is required, such as bonding dissimilar or thermally sensitive materials.

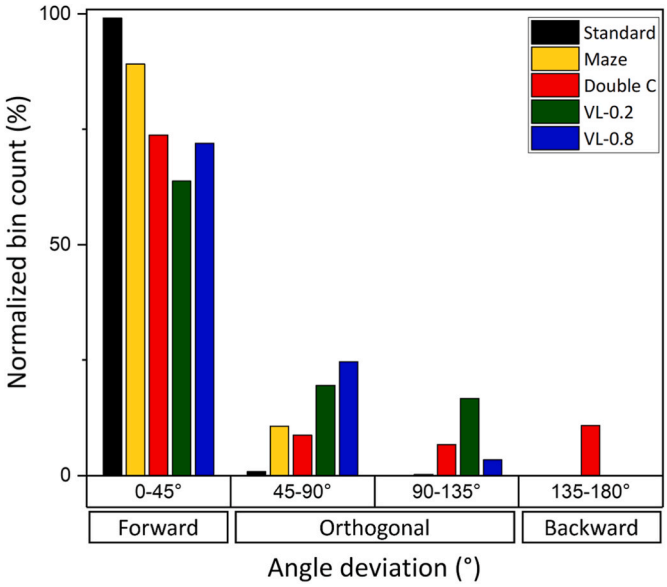

Fig. 18. Normalized angular deviation of local propagation vectors for all samples. Angles were grouped into four bins (0–45°, 45–90°, 90–135° and 135–180°) to quantify directional changes during reaction propagation. For each sample, the number of vectors in each angle bin was normalized by the total number of vectors and expressed as a percentage.

CRediT authorship contribution statement

Maria Amélia Martins: Writing – original draft, Visualization, Validation, Methodology, Investigation, Formal analysis, Data curation, Conceptualization. **Christian Singer:** Writing – review & editing, Methodology. **Tim Dahmen:** Writing – review & editing, Supervision, Resources. **Frank Mücklich:** Writing – review & editing, Supervision, Resources, Project administration, Funding acquisition. **Christoph Pauly:** Writing – review & editing, Supervision, Conceptualization.

Declaration of competing interest

The authors declare that they have no known competing financial interests or personal relationships that could have appeared to influence the work reported in this paper.

Acknowledgement

The authors wish to acknowledge funding from the Deutsche Forschungsgemeinschaft (DFG), project number 426339810, and support for the femtosecond laser Solstice ACE, project number 467354208. Maria Amélia Martins gratefully acknowledges financial support from the Roberto Rocca Education Program (RREP). The authors also thank Augusto Ribeiro Castro for his initial contributions to the image analysis concept, which laid the groundwork for the development of the methodology used in this study.

Appendix A. Supplementary data

Supplementary data to this article can be found online at https://doi.org/10.1016/j.mtadv.2025.100648.

7. Supplementary Information

https://doi.org/10.5281/zenodo.16949158 (High-speed camera videos).

https://cloud.dfki.de/owncloud/index.php/s/nHWMwcSxqbeRM6M (Source Code).

Data availability

Data will be made available on request.

References

[1] A.S. Rogachev, Exothermic reaction waves in multilayer nanofilms, Russ. Chem. Rev. 77 (1) (2008) 21–37.

[2] D.P. Adams, Reactive multilayers fabricated by vapor deposition: a critical review, Thin Solid Films 576 (2015) 98–128, https://doi.org/10.1016/j.tsf.2014.09.042 [Internet].

[3] A.S. Rogachev, A.S. Mukasyan, Combustion of heterogeneous nanostructural systems, Combust. Explos. Shock Waves 46 (3) (2010) 243–266.

[4] Q. Bizot, O. Politano, A.A. Nepapushev, S.G. Vadchenko, A.S. Rogachev, F. Baras, Reactivity of the Ti-Al system: experimental study and molecular dynamics simulations, J. Appl. Phys. 127 (14) (2020 Apr 14) 145304 [Internet][cited 2021 Mar 25]Available from: http://aip.scitation.org/doi/10.1063/5.0004550.

[5] B. Boettge, J. Braeuer, M. Wiemer, M. Petzold, J. Bagdahn, T. Gessner, Fabrication and characterization of reactive nanoscale multilayer systems for low-temperature bonding in microsystem technology, J. Micromech. Microeng. 20 (6) (2010).

[6] J. Braeuer, T. Gessner, A hermetic and room-temperature wafer bonding technique based on integrated reactive multilayer systems, J. Micromech. Microeng. 24 (11) (2014).

[7] A.S. Rogachev, Reactive multilayer nanofilms: time of scientific and technological maturity, Russ. Chem. Rev. 93 (1) (2024) RCR5106.

[8] J. Wang, E. Besnoin, A. Duckham, S.J. Spey, M.E. Reiss, O.M. Knio, et al., Room-temperature soldering with nanostructured foils, Appl. Phys. Lett. 83 (19) (2003) 3987–3989.

[9] T.P. Weihs, Fabrication and characterization of reactive multilayer films and foils, in: Metallic Films for Electronic, Optical and Magnetic Applications: Structure, Processing and Properties, 2013, pp. 160–243.

[10] K. Woll, A. Bergamaschi, K. Avchachov, F. Djurabekova, S. Gier, C. Pauly, et al., Ru/Al multilayers integrate maximum energy density and ductility for reactive materials, Sci. Rep. 6 (July 2015) (2016) 1–10, https://doi.org/10.1038/srep19535 [Internet].

[11] S.Q. Arlington, G.M. Fritz, T.P. Weihs, Exothermic formation reactions as local heat sources, Annu. Rev. Mater. Res. 52 (2022) 219–248.

[12] A. Wang, I. Gallino, S.S. Riegler, Y.T. Lin, N.A. Isaac, Y.H. Sauni Camposano, et al., Ultrafast formation of single phase B2 AlCoCrFeNi high entropy alloy films by reactive Ni/Al multilayers as heat source, Mater Des [Internet] 206 (2021 Aug 1) 109790 [cited 2021 May 21]Available from: https://linkinghub.elsevier.com/retrieve/pii/S0264127521003439.

[13] M. Glaser, S. Matthes, J. Hildebrand, J. Pierre Bergmann, P. Schaaf, Hybrid thermoplastic-metal joining based on Al/Ni multilayer foils – analysis of the joining zone, Mater Des 226 (2023) 111561, https://doi.org/10.1016/j.matdes.2022.111561.

[14] A.J. Swiston, T.C. Hufnagel, T.P. Weihs, Joining bulk metallic glass using reactive multilayer foils, Scr. Mater. 48 (12) (2003) 1575–1580.

[15] A. Duckham, S.J. Spey, J. Wang, M.E. Reiss, T.P. Weihs, E. Besnoin, et al., Reactive nanostructured foil used as a heat source for joining titanium, J. Appl. Phys. 96 (4) (2004) 2336–2342.

[16] B. Rheingans, R. Furrer, I. Spies, A. Schumacher, S. Knappmann, L.P.H. Jeurgens, et al., Reactive joining of thermally and mechanically sensitive materials, J. Electron. Packag. 140 (2018) 1–17.

[17] A. Jung, C. Pauly, P. Schaaf, Reactive multilayers, their design and their applications: bonding, debonding, repair, recycle, Adv. Eng. Mater. 27 (3) (2025) 2024–2026.

[18] G.M. Fritz, S.J. Spey, M.D. Grapes, T.P. Weihs, Thresholds for igniting exothermic reactions in Al/Ni multilayers using pulses of electrical, mechanical, and thermal energy, J. Appl. Phys. 113 (1) (2013).

[19] C. Luo, Y. Zhang, Joining of copper foils via Al/Ni reactive multilayer nanofoils, J. Mater. Process. Technol. 298 (July) (2021) 117294, https://doi.org/10.1016/j.jmatprotec.2021.117294.

[20] S. Kanetsuki, S. Miyake, T. Namazu, Effect of Free-standing Al / Ni Exothermic Film on Thermal Resistance of Reactively Bonded Solder Joint 31 (3) (2019) 729–741.

[21] J. Subrahmanyam, M. Vijayakumar, Self-propagating high-temperature synthesis, J. Mater. Sci. 27 (23) (1992) 6249–6273.

[22] T.P. Weihs, Self-propagating reactions in multilayer materials, in: Handbook of Thin Film Process Technology, 1997.

[23] E.G. Gamaly, A.V. Rode, Physics of ultra-short laser interaction with matter: from phonon excitation to ultimate transformations, Prog Quantum Electron [Internet] 37 (5) (2013) 215–323, https://doi.org/10.1016/j.pquantelec.2013.05.001.

[24] D. Neely, R. Allott, B. Bingham, J. Collier, J. Greenhalgh, M. Michaelis, et al., Energy coupling in short pulse laser solid interactions and its impact for space debris removal, Appl. Opt. 53 (31) (2014) I41.

[25] M.D. Shirk, P.A. Molian, A review of ultrashort pulsed laser ablation of materials | Browse -, Journal of Laser Applications. JlaAipOrg [Internet] 10 (1) (1998) 18–28. Available from: http://jla.aip.org/resource/1/jlapen/v10/i1/p18_s1%5Cnpapers3://publication/uuid/40DB51D4-9B7D-4875-A5C3-0B20EEAC8D03.

[26] M.A. Martins, D.W. Müller, J. Schmauch, M. Glaser, J.P. Bergmann, F. Mücklich, et al., Effects of ultrashort pulsed direct laser writing on Ni/Al reactive multilayer foils, Appl. Sci. 13 (7) (2023) 4313.

[27] S.I. Kudryashov, B. Gakovic, P.A. Danilov, S.M. Petrovic, D. Milovanovic, A. A. Rudenko, et al., Single-shot selective femtosecond laser ablation of multi-layered Ti/Al and Ni/Ti films: "cascaded" heat conduction and interfacial thermal effects, Appl. Phys. Lett. 112 (2) (2018), https://doi.org/10.1063/1.5010793 [Internet].

[28] J. Cheng, W. Perrie, S.P. Edwardson, E. Fearon, G. Dearden, K.G. Watkins, Effects of laser operating parameters on metals micromachining with ultrafast lasers, Appl. Surf. Sci. 256 (5) (2009) 1514–1520.

[29] B.N. Chichkov, C. Momma, S. Nolte, F. von Alvensleben, A. Tünnermann, Femtosecond, picosecond and nanosecond laser ablation of solids, Appl. Phys. A Mater. Sci. Process. 63 (2) (1996) 109–115.

[30] A. Tünnermann, C. Momma, S. Nolte, Perspective on ultrashort pulse laser micromachining, Appl Phys A Mater Sci Process [Internet] 129 (2) (2023) 1–3, https://doi.org/10.1007/s00339-023-06403-9.

[31] Y.N. Picard, D.P. Adams, J.A. Palmer, S.M. Yalisove, Pulsed laser ignition of reactive multilayer films, Appl. Phys. Lett. 88 (14) (2006 Apr 3).

[32] Y.N. Picard, H.H. Liu, S.J. Speys, J.P. McDonald, D.P. Adams, T.P. Weihs, et al., Cutting reactive foils without igniting them (a femtosecond laser machining approach), Mater. Res. Soc. Symp. Proc. 800 (2003) 387–392.

[33] Y.N. Picard, D.P. Adams, S.M. Yalisove, Femtosecond laser interactions with Co/Al multilayer films, Mater. Res. Soc. Symp. Proc. 850 (2005) 115–121.

[34] Y.N. Picard, S.M. Yalisove, Femtosecond laser heat affected zones profiled in CoSi multilayer thin films, Appl. Phys. Lett. 92 (1) (2008) 1–4.

[35] M.A. Martins, C. Schäfer, F. Mücklich, C. Pauly, Influence of oxide formation following ultrashort pulsed laser micromachining on self-propagating reactions in free-standing Ni/Al reactive multilayer foils, Adv. Eng. Mater. (2024) 2400215, 1–10.

[36] Y.H.S. Camposano, H. Bartsch, S. Matthes, M. Oliva-ramirez, K. Jaekel, P. Schaaf, Microstructural Characterization and Self-Propagation Properties of Reactive Al / Ni Multilayers Deposited onto Wavelike Surface Morphologies : in Fl Uence on the Propagation Front Velocity, 2023 2200765.

[37] Y.H. Sauni Camposano, K. Jaekel, S.S. Riegler, S. Matthes, M. Glaser, N.J. Peter, et al., Controlling propagation velocity in Al/Ni reactive multilayer systems by periodic 2D surface structuring, Adv. Eng. Mater. (2024) 2302272, 1–11.

[38] S. Danzi, M. Menétrey, J. Wohlwend, R. Spolenak, Thermal management in Ni/Al reactive multilayers: understanding and preventing reaction quenching on thin film heat sinks, ACS Appl. Mater. Interfaces 11 (2019) 42479–42485.

[39] D. Shekhawat, M. Breiter, J. Döll, F. Daneshpazhooneja, A. Jung, J. Pezoldt, Transfer of self-sustained reactions between thermally coupled reactive material elements, Adv. Eng. Mater. (2024) 53–56.

[40] J.P. McDonald, V.C. Hodges, E.D. Jones, D.P. Adams, Direct observation of spinlike reaction fronts in planar energetic multilayer foils, Appl. Phys. Lett. 94 (3) (2009).

[41] S. Matthes, M. Glaser, E. Vardo, Y.H. Sauni Camposano, K. Jaekel, J.P. Bergmann, et al., Tailoring the reaction path: external crack initiation in reactive Al/Ni multilayers, Adv. Eng. Mater. (2024) 2302271.

[42] H. Li, Y. Ma, B. Xu, D. Bridges, L. Zhang, Z. Feng, et al., Laser welding of Ti6Al4V assisted with nanostructured Ni/Al reactive multilayer films, Mater. Des. (2019) 181.

[43] E.R. Wainwright, K.T. Sullivan, M.D. Grapes, Designer direct ink write 3D-Printed thermites with tunable energy release rates, Adv. Eng. Mater. 22 (6) (2020) 1–7.

[44] E. Tichtchenko, A. Estève, C. Rossi, Modeling the self-propagation reaction in heterogeneous and dense media: application to Al/CuO thermite, Combust. Flame 228 (2021 Jun 1) 173–183.

[45] Product data sheet. Indium corporation 86 (2021) 580400, 98569.

[46] H.E. Lü, P.S.P. Wang, A fast parallel algorithm for thinning digital patterns, Commun. ACM 29 (3) (1986) 239–242.

[47] J. Canny, A computational approach to edge detection, IEEE Trans. Pattern Anal. Mach. Intell. PAMI-8 (6) (1986) 679–698.

[48] P.H.C. Eilers, B.D. Marx, Flexible smoothing with B-splines and penalties, Stat. Sci. 11 (2) (1996) 89–102.

[49] C.A. Schneider, W.S. Rasband, K.W. Eliceiri, NIH image to ImageJ: 25 years of image analysis, Nat. Methods 9 (7) (2012) 671–675.

[50] Y.H. Sauni Camposano, K. Jaekel, S.S. Riegler, S. Matthes, M. Glaser, N.J. Peter, et al., Controlling propagation velocity in Al/Ni reactive multilayer systems by periodic 2D surface structuring, Adv. Eng. Mater. (2024) 2302272, 1–11.

[51] T. Wang, Q. Zeng, M. Li, Characterization and application of Al/Ni reactive multilayers in exploding foils, Cent. Eur. J. Energ. Mater. 14 (3) (2017) 547–558.

[52] A.B. Mann, A.J. Gavens, M.E. Reiss, D. Van Heerden, G. Bao, T.P. Weihs, Modeling and characterizing the propagation velocity of exothermic reactions in multilayer foils, J. Appl. Phys. 82 (3) (1997) 1178–1188.

[53] A.J. Gavens, D. Van Heerden, A.B. Mann, M.E. Reiss, T.P. Weihs, Effect of intermixing on self-propagating exothermic reactions in Al/Ni nanolaminate foils, J. Appl. Phys. 87 (3) (2000) 1255–1263.
[54] S. Danzi, V. Schnabel, X. Zhao, J. Käch, R. Spolenak, Architecture-independent reactivity tuning of Ni/Al multilayers by solid solution alloying, Appl Phys Lett [Internet] 114 (18) (2019 May 6) 183102 [cited 2021 Mar 17] Available from: http://aip.scitation.org/doi/10.1063/1.5095828.
[55] D. Shekhawat, M. Baloochi, D. Sudhahar, V.A. Raheja, J. Döll, H.O. Jacobs, et al., Influence of environment on self-propagating reactions in Al/Ni multilayer foils, MRS Adv 8 (9) (2023) 477–483, https://doi.org/10.1557/s43580-023-00574-6 [Internet].
[56] M.J. Abere, R.V. Reeves, D.E. Kittell, C. Sobczak, D.P. Adams, Stability criteria for self-propagating reaction waves in Co/Al multilayers, ACS Appl. Mater. Interfaces 15 (17) (2023) 21210–21218.
[57] D.E. Kittell, M.J. Abere, C.D. Yarrington, D.P. Adams, 3D simulations of spinlike flames in Co/Al multilayers with enhanced conduction losses, Combust Flame [Internet] 240 (2022) 111952, https://doi.org/10.1016/j.combustflame.2021.111952.
[58] Y.C. Chen, Y.W. Chang, C.C. Hsiang, Y.P. Chiu, K.W. Su, Y.C. Chou, Control of self-propagating reactions and phases in Ni/Si reactive multilayers, J Mater Chem C Mater 13 (10) (2025) 5073–5084.